241 (2024) 213186

Contents lists available at ScienceDirect

Geoenergy Science and Engineering

journal homepage: www.sciencedirect.com/journal/geoenergy-science-and-engineering

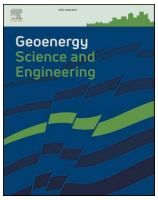

Proppant transport in secondary Sand fracturing using Eulerian-Eulerian multiphase model Approach

Huohai Yang [a], Kuncheng Li [a], Zijia Liao [b,**], Xiaogang Li [a], Hesamoddin Rabiee [c], Shirui Ren [a], Xinwei Luo [a], Qingyuan Chen [a,b], Lei Ge [c,*], Hao Wang [c]

[a] State Key Laboratory of Oil and Gas Reservoir Geology and Exploitation, Southwest Petroleum University, Chengdu, 610500, China
[b] Tianfu Yongxing Laboratory, Chengdu, 610213, China
[c] Centre for Future Materials, University of Southern Queensland, Springfield, QLD, 4300, Australia

ARTICLE INFO

Keywords:
Secondary sand fracturing
Eulerian-Eulerian multiphase model
Sanding index
Fluid flow rate
Sand ratio

ABSTRACT

Secondary sand fracturing, an innovative hydraulic fracturing technique, divides the injection of proppant into two stages, altering the reservoir's rock mechanics and fracturing fluid flow paths, thus effectively controlling fracture creation and improving the effectiveness of proppant placement. This methodology facilitates fracture height control and enhances fracture conductivity, benefiting production rate. Despite abundant literature on proppant transport, limited attention has been paid to exploring the specific aspects of secondary sand fracturing. In this study, the Eulerian-Eulerian multiphase model was used to simulate the proppant transport in secondary sand fracturing for the first time. This model accounts for turbulence and the interplay between proppant particles, thus enabling a comprehensive integration of fluid and particulate phases. The effects of proppant performance, fracturing fluid performance, and fluid flow rate on proppant placement were analyzed. In the first sand-addition stage, an innovative sanding index was proposed to evaluate the effectiveness of proppant placement. Combined with the orthogonal experiment, the fluid flow rate significantly influences proppant placement. An escalated flow rate augments both the sandbank leading edge and laying lengths, concurrently diminishing the equilibrium height and the sanding index. In the second sand-addition stage, the equilibrium height increases with the increase of sand ratio, decreases with the increase of flow rate and fluid viscosity, and first increases and then decreases with the increase of particle size and proppant density. This study enriches the comprehension of proppant placement and its governing elements within hydraulic fracturing, thereby furnishing a more empirical and theoretically sound foundation for optimizing secondary sand fracturing practices.

Nomenclature

t	Time , s	μ_l	Dynamic viscosity of the liquid phase, Pa·s
α_s	The volume fraction of the solid phase, dimensionless	C_D	The interphase momentum exchange coefficient, dimensionless
α_l	Liquid fraction of solid phase, dimensionless	ε_l	Turbulence dissipation rate, m^2/s^3
ρ_s	Proppant density, kg/m^3	ϕ	The sand ratio, %
ρ_l	Fluid density, kg/m^3	M	Sanding index, dimensionless
v_s	The velocity of proppant, m/s	L_{AQ}	The sandbank laying length, m

(*continued on next column*)

(*continued*)

v_l	The velocity of fluid, m/s	L_{EQ}	The sandbank leading edge length, m
p_s	The pressure of the proppant phase, Pa	H_{EQ}	The sandbank equilibrium height, m
p_l	The pressure of the fluid phase, Pa	α_s^{max}	The maximum accumulated volume fraction of particles, value = 0.63
τ_s	The shear stress tensor of the solid phase, Pa	A_{EQ}	The area of the sandbank, m^2
τ_l	The shear stress tensor of the fluid phase, Pa	A_{LF}	The area of the crack plate, m^2
g	The acceleration due to gravity, m/s^2	$X_i(k)$	The dimensionless mean value of the i_{th} parameter is the parameter of

(*continued on next page*)

* Corresponding author.
** Corresponding author.
E-mail addresses: lzjfrac@foxmail.com (Z. Liao), lei.ge@unisq.edu.au (L. Ge).

https://doi.org/10.1016/j.geoen.2024.213186
Received 21 March 2024; Received in revised form 5 June 2024; Accepted 25 July 2024
Available online 26 July 2024

(*continued*)

			the serial number, k is the data serial number
β	The inter-phase momentum exchange coefficient, $kg{\cdot}m^{-3}{\cdot}s^{-1}$	$x_i(k)$	The i_{th} parameter value,
σ_κ	The Prandtl number for turbulent kinetic energy, value = 1.0	$\overline{x_i}$	The arithmetic mean
σ_ε	The Prandtl number for the turbulent dissipation rate, value = 1.3	$\xi_i(k)$	The grey relational coefficient, dimensionless
$C_{1\varepsilon}$	Empirical constant, value = 1.44	ρ	Distinguishing coefficient, value = 0.5
$C_{2\varepsilon}$	Empirical constant, value = 1.92	γ_i	The degree of correlation degree
k_s	Particle relaxation time, s	W_i	The weight coefficient, dimensionless
d_s	Proppant diameter, m		

1. Introduction

The global imperative for cleaner, low-carbon energy solutions has intensified in response to growing concerns about climate change and environmental sustainability. This push to transition from traditional fossil fuels to more environmentally friendly alternatives has spotlighted natural gas as a crucial player in the pursuit of cleaner energy sources (ABDIN, Z, 2024; Sanya and Konisky, 2020). Central to natural gas extraction from unconventional reservoirs is the revolutionary technology of hydraulic fracturing, colloquially known as "fracking". The process starts with the high-pressure injection of fracturing fluid into the wellbore to create fractures, followed by the injection of fracturing fluid with proppant such as quartz sand or ceramic to create high-conductivity channels from the reservoir to the wellbore, enabling the flow of oil and gas, thus achieving increased production (CAO, H et al., 2024; CHEN, B et al., 2022; LIAO, Z et al., 2022). For some special reservoirs, such as bottom water reservoirs, the conventional hydraulic fracturing technique faces challenges, such as uncontrolled fracture height and low effective fracture conductivity (LAI, F et al., 2017; Prasun and Ghalambor, 2018, Shi et al., 2018; ZHAO, J et al., 2019). Consequently, several researchers have proposed the concept of secondary sand fracturing. Unlike the conventional hydraulic fracturing technique that injects proppant into the formation in one stage, the secondary sand technique divides proppant injection into two stages. As shown in Fig. 1, in the first sand-addition stage, fracturing fluid containing proppant was injected; after a pumping pause, the proppant settled within the fractures, forming an artificial barrier. In the second sand-addition stage, additional proppant was injected, resulting in larger volumes of propped fractures (Li et al., 2009). Compared to the conventional hydraulic fracturing technique, secondary sand fracturing has the following advantages.

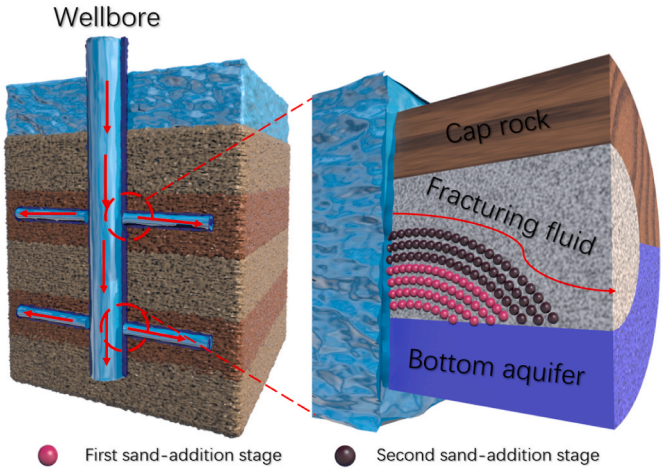

Fig. 1. Schematic diagram of secondary sand fracturing.

(1) For bottom water reservoirs, after injecting the proppant in the sand-addition stage, the proppant formed an artificial barrier at the bottom of the fractures to control downward extension and prevent infiltration into the underlying aquifer.
(2) The presence of an artificial barrier hinders the vertical extension of fractures, promoting the proppant flow towards the far end of the fractures during the second sand-addition stage. This leads to higher proppant concentration and propped fracture volume, thereby improving effective fracture conductivity.
(3) It reduces the risk of sand plugging due to a faster rate of fracture volume growth, increases the success rate of construction, and improves the production enhancement effect of hydraulic fracturing.

For instance, in China's HeShun Gas Field, a secondary sand fracturing technique was employed in 10 wells to address the challenge of fractures efficiently communicating with underlying aquifers, with construction efficiency reaching 90%. Compared to neighboring wells that use the conventional fracturing technique, natural gas production increases by 60%, and the liquid-to-gas ratio decreases by 31.7% (XU, Bingwei et al., 2022). In the East China Sea, offshore gas fields showed that, during the same period, the initial production of the target doubled compared to neighboring wells, while the cumulative production increased threefold, indicating a significant improvement in the production owing to the employment of secondary sand fracturing (Y, Feng-Sheng et al., 2020).

In the process of secondary sand fracturing, the placement of proppant within the fractures is crucial because it directly affects the fracture conductivity and determines the productivity of oil and gas wells, thereby impacting the post-fracturing production (MAO, S et al., 2020; SHI, F et al., 2018). For example, RAIMBAY, A et al. (2016) conducted experimental research on the impacts of rock surface roughness and fracturing fluid type on proppant transport and found that polymer-based fracturing fluids, compared to water, were more conducive to proppant transport in rough fractures. The smoother the rock surface, the more proppant tended to be uniformly distributed in multiple layers, resulting in lower fracture conductivity. WEN, Q et al. (2016) experimentally studied the effects of fluid viscosity and fracture complexity on proppant transport. The study demonstrated that to improve the fracture conductivity, we can choose low-viscosity fluids to carry the proppant or high-viscosity fluids to carry the proppant to support the fractures that extend away from the wellbore. Li et al. (2022) developed a triaxial fracking experimental system to obtain a more realistic distribution of proppant during hydraulic fracturing, with the results indicating that the stress required for proppant transport in horizontal fractures was lower than that in vertical fractures.

In addition to physical experiments, numerical simulation is also vital for studying proppant transport due to its efficiency, cost-effectiveness, and ability to precisely control variables. Nowadays, the Eulerian-Lagrangian multiphase method and the Eulerian-Eulerian multiphase method are the most widely used method to study multiphase problems. In the Eulerian-Lagrangian method, the fluid phase is treated as a continuous phase, while the particle phase is treated as a discrete phase. The motion trajectories of the particles are independently calculated using Newton's laws, primarily addressing the microscopic movement state and trajectories of the particles(WEN, Z et al., 2022). For example, YI, S S et al. (2018) modeled the proppant distribution using CFD-DEM in multiple perforation clusters during a hydraulic fracture operation, with the results indicating that if toe-side clusters screen out at an early proppant stage, the fluid and proppant are redistributed to the heel-side clusters. ZENG, J et al. (2019) coupled the crack propagation model with the proppant transport model, solved

the crack propagation model using the PKN model, and simulated the transport of proppant in the extended crack using the Eulerian-Lagrangian method. MAO, S et al. (2023) also conducted similar research. The Eulerian-Lagrangian model requires the volume fraction of the solid phase to be much smaller. This characteristic limits the range of sand ratios that can be simulated in proppant transport within fractures, making it unsuitable for simulating high sand ratio fracturing fluids. This limitation is particularly significant for secondary sand fracturing, where the proppant concentration is relatively high. In contrast, the Eulerian-Eulerian multiphase model treats the solid phase as a pseudo-fluid and sets the sum of the volume fractions of all phases to be 1. By deriving the momentum and mass conservation equations for each phase, it can address the simulation of proppant transport at high sand ratios. This method has recently been used to study the transport and settling behavior of proppants in hydraulic fracturing. For example, YANG, R et al. (2019) studied the proppant transport in complex fracture networks using an Eulerian-Eulerian method and revealed that in the fracture network system, proppant mainly accumulated in the primary and secondary fractures near the primary fractures. However, limited proppants were present in the deep part of the fracture system, rendering ineffective support for the deep regions of the complex fracture system. Li et al., (2023)studied the pulse effect mechanism and regularity on the proppant transport in fracture using an Eulerian-Eulerian method and revealed that pulse injection can extend the migration range of proppants, and the range extension effect is only significant when the pulse amplitude is greater than 0.3 m/s.

Herein, it is proposed to harness numerical simulation to investigate the distribution of proppant during the secondary sand addition process, which can lead to improved hydraulic fracturing techniques and overall reservoir performance. Despite the abundance of literature concerning proppant transport, the investigation into the nuanced aspects of secondary sand fracturing has been significantly limited, particularly regarding the impact of the artificial barrier formed in the first sand-addition stage on the proppant transport in the second sand-addition stage. Considering the research objectives and computational costs, an Eulerian-Eulerian multiphase method was established, and commercial software FLUENT was used to investigate the effects of factors such as sand ratio, proppant size, proppant density, fluid flow rate, fluid viscosity, and fluid density on proppant transport in secondary sand fracturing for the first time. The findings obtained provide a more scientific and reasonable theoretical design basis for secondary sand fracturing.

2. Model approach

2.1. Mathematical model

The Eulerian- Eulerian multiphase flow model was used to simulate the proppant transport based on the following assumptions.

(1) In the Eulerian-Eulerian multiphase flow model, the particle phase is treated as a pseudo-fluid coupled with the fluid phase. Each phase satisfies the conservation of momentum and mass.
(2) The fluid flow within the fracture was characterized as unsteady.
(3) The proppant particles exhibited uneven sizes; however, the average particle size was typically used.

Continuity equation:

$$\frac{\partial}{\partial t}(\alpha_l\rho_l)+\nabla\cdot(\alpha_l\rho_l v_l)=0 \tag{1}$$

$$\frac{\partial}{\partial t}(\alpha_s\rho_s)+\nabla\cdot(\alpha_s\rho_s v_s)=0 \tag{2}$$

Momentum equation:

$$\frac{\partial}{\partial t}(\alpha_l\rho_l v_l)+\nabla\cdot(\alpha_l\rho_l v_l v_l)=-\alpha_l\nabla p_l+\nabla\cdot\tau_l+\alpha_l\rho_l g+\beta(v_s-v_l) \tag{3}$$

$$\frac{\partial}{\partial t}(\alpha_s\rho_s v_s)+\nabla\cdot(\alpha_s\rho_s v_s v_s)=-\alpha_s\nabla p_s+\nabla\cdot\tau_s+\alpha_s\rho_s g+\beta(v_l-v_s) \tag{4}$$

where t represents time (s), α_s and α_l represent the volume fraction of the solid phase and liquid phase, respectively(dimensionless), ρ_s and ρ_l represent the density of solid phase and liquid phase, respectively (kg/m^3), v_s and v_l represent the velocity of solid phase and liquid phase, respectively (m/s), p_s and p_l represents the pressure of solid phase and liquid phase, respectively (Pa), τ_s and τ_l represents the shear stress tensor of the solid phase and liquid phase, respectively (Pa), g represents the acceleration due to gravity (m/s^2), β represents the inter-phase momentum exchange coefficient (kg·m^{-3}·s^{-1})

Owing to the narrow fracture width and rough wall, significant momentum exchange occurred between the solid and liquid phases in the flow of the fracturing fluid within the fracture. Therefore, the flow of the fracturing fluid inside the fracture was turbulent. The k-ε model (GUO, T et al., 2022; TIANKUI, G et al., 2023) is commonly used to describe this turbulent characteristic, and the mathematical equations for the turbulent flow and turbulent diffusion equations in this model are as follows(ZHANG, J et al., 2023):

$$\frac{\partial}{\partial t}(\rho_m k)+\nabla\cdot\left(\rho_m\vec{V}_m k\right)=\nabla\cdot\left(\left(\mu_m+\frac{\mu_{t,m}}{\sigma_k}\right)\nabla k\right)+G_{k,m}-\rho_m\epsilon+\Pi_{k_m} \tag{5}$$

$$\frac{\partial}{\partial t}(\rho_m\varepsilon)+\nabla\cdot\left(\rho_m\vec{V}_m\varepsilon\right)=\nabla\cdot\left(\left(\mu_m+\frac{\mu_{t,m}}{\sigma_\varepsilon}\right)\nabla\varepsilon\right)+\frac{\varepsilon}{k}\left(C_{1\varepsilon}G_{k,m}-C_{2\varepsilon}\rho_m\varepsilon\right)+\Pi_{\varepsilon_m} \tag{6}$$

where σ_κ is the Prandtl number for turbulent kinetic energy and has a value of 1.0, σ_ε is the Prandtl number for the turbulent dissipation rate and has a value of 1.3, $C_{1\varepsilon}$ and $C_{2\varepsilon}$ are empirical constants, with values of 1.44 and 1.92, respectively.

The interphase exchange coefficient K_{sl} is used to describe the interaction and exchange processes between the solid and liquid phases. It represents the rate of exchange of physical quantities such as mass, momentum, and energy between the solid and liquid phases in the solid-liquid two-phase flow:

$$K_{sl}=\frac{\alpha_s\rho_s f}{\mathrm{k}_s} \tag{7}$$

where k_s represents the particle relaxation time(s), which reflects the time required for the particles to reach equilibrium from their initial state under the influence of external forces or fluid flow:

$$\mathrm{k}_s=\frac{\rho_s d_s^2}{18\mu_l} \tag{8}$$

where d_s represents the particle diameter of the solid phase (m), μ_l represents the dynamic viscosity of the liquid phase (Pa·s), f is related to the drag function, and it is calculated using the Gidaspow model(GONG, Y et al., 2020; SURI, Y et al., 2019).

When $\alpha_s \le 0.2$, the inter-phase exchange coefficient K_{sl} can be described as:

$$K_{sl}=\frac{3}{4}C_D\frac{\alpha_s\alpha_l\rho_l|v_s-v_l|}{d_s}\alpha_l^{-2.65} \tag{9}$$

When $\alpha_s > 0.2$, the inter-phase exchange coefficient K_{sl} can be described as:

$$K_{sl}=150\frac{\alpha_s(1-\alpha_l)\mu_l}{\alpha_l d_s^2}+1.75\frac{\rho_l\alpha_s|v_s-v_l|}{d_s} \tag{10}$$

$$C_D = \begin{cases} \frac{24}{Re_s}\left[1 + 0.15(Re_s)^{0.687}\right] & Re_s < 1000 \\ 0.44 & Re_s \geqslant 1000 \end{cases} \quad (11)$$

$$Re_s = \frac{\rho_l d_s \varepsilon_l |v_s - v_l|}{\mu_l} \quad (12)$$

where C_D represents the interphase momentum exchange coefficient (dimensionless), Re_s is the Reynolds number defined by the interphase slip velocity (dimensionless), d_s is the diameter of the solid phase particles (m), and ε_l is the turbulence dissipation rate (m^2/s^3).

The inlet boundary condition for simulating the crack adopts a velocity inlet, with the parameter set as the radial flow velocity of the fracturing fluid at the interface of the crack inlet. The outlet boundary condition is set as the pressure outlet, and the standard atmospheric pressure of 101.325 kPa is taken as the outlet pressure. The model has a gravity acceleration of −9.81 m/s^2, a wall roughness of 0, and no slip.

2.2. Simulation conditions

Using an Eulerian-Eulerian multiphase flow model, this study investigated the proppant transport within hydraulic fractures. According to the process of secondary sand fracturing, the proppant transport is divided into three parts.

(1) The first sand-addition stage, as shown in Fig. 2a, in which the geometric crack model is simplified as a flat plate. The size of the flat plate is fixed and will not change due to changes in the fracturing fluid and proppant factors. According to the similarity criterion, the crack's length, height, and width in the numerical model were scaled down to 4 m, 0.4 m, and 0.01 m, respectively. These scaled dimensions represent the actual underground crack, which has a length of 200 m, a height of 20 m, and a width of 0.01 m. In the simulation, fluid was injected from the left boundary of the crack. The entrance was located on the left side of the crack model (height: 0.04m, with the middle of the entrance located at the center of the crack height). Ten equally wide outlets were set at the fracturing fluid outlet with a height of 0.02 m and evenly distributed on the model's right side. The fracturing fluid outlet was set with 10 equally wide outlets (height: 0.02 m) evenly distributed on the model's right side. The grid size is divided into 0.01 m, and the crack is divided into 32080 grid units.

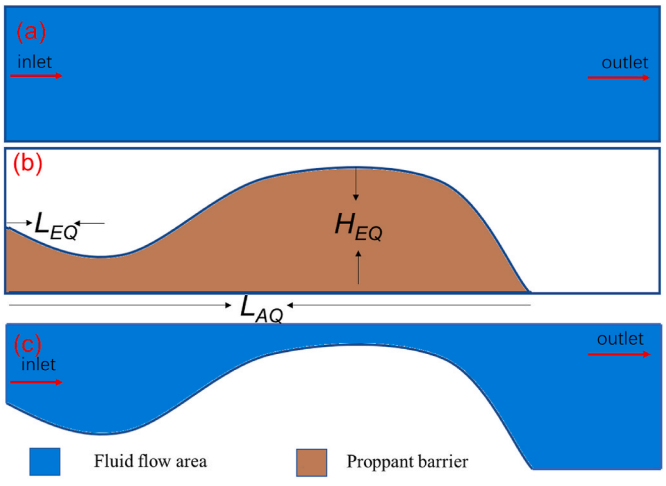

Fig. 2. Schematic diagram of crack geometry and boundary conditions: (a) The First Sand Addition stage, (b) Pumping pause and forming an artificial barrier, (c)The Second Sand Addition stage.

(2) Pumping pause: the proppant settled within the fractures, forming an artificial barrier, as shown in Fig. 2b.
(3) Second sand-addition stage: this research assumes that the sandbank obtained from the first sand-addition stage remains at a fixed boundary and is not affected by the scouring of the fracturing fluid during the second sand-addition stage, as shown in Fig. 2c.

2.3. Characterization parameters and experiment design

The proppant placement during the first sand-addition process was extracted, as shown in Fig. 2b, wherein L_{EQ} is the sandbank leading-edge length, representing the filling effect of the proppant in the near-wellbore zone. If L_{EQ} is too large, the proppant does not settle at the fracture entrance near the wellbore; this ineffective filling can lead to crack closure. Even with well-placed proppant placed further down the fracture, the hydraulic fracturing effectiveness remains poor. H_{EQ} is the sandbank equilibrium height, representing the height of the sandbank when it reaches dynamic equilibrium during proppant migration in the fracture. This parameter reflects the final effect of proppant placement in the fracture. A larger H_{EQ} means more proppant has settled in the fracture, providing better oil and gas flow channels and increasing fracture conductivity. L_{AQ} is the sandbank laying length, representing the distance from the farthest end of the sandbank to the entrance of the fracture. This parameter indicated the proppant's filling effect in the fracture's remote well zone. In other words, it reflects the extent to which the proppant has spread within the fracture, affecting the conductivity and flow paths in more distant regions of the fracture. In addition, we propose a sanding index through cluster analysis and dimensional analysis that can be used to quantify the proppant placement comprehensively. The Sanding index can be described as:

$$M = \frac{\alpha_s^{max} A_{EQ} C_1 (C_2 L_{AQ} - C_3 L_{EQ})^2}{A_{LF} C_4 H_{EQ} C_5 L_{EQ}} \quad (13)$$

where M is sanding index (dimensionless); C_1, C_2, C_3, C_4, C_5 are weight coefficients that can focus on different factors for evaluation (dimensionless), taking a value of 1 in this study; L_{AQ} is the sandbank laying length(m); L_{EQ} is the sandbank leading edge length(m); H_{EQ} is the sandbank equilibrium height (m); α_s^{max} is the maximum accumulated volume fraction of particles (dimensionless), taking a value of 0.63; A_{EQ} is the area of the sandbank (m^2); A_{LF} is the area of the crack plate (m^2).

In the first sand-addition stage, orthogonal experimental design is used to study the proppant transport. The orthogonal experimental method is a design approach used to examine multiple factors at various levels (GONG, F et al., 2023; Li and Hao, 2020). The design of orthogonal experiments has proven to be a highly efficient, fast, and economical experimental method for evaluating the effects of different factors on performance (ZOU, G et al., 2017). The design of orthogonal experiments was based on using orthogonal tables. In orthogonal experiments, the factors represent the parameters influencing proppant transport, whereas the levels refer to the maximum number of values that each factor can assume. By understanding the importance of various factors and their interactions, the main advantage of this method is that it reduces the number of required tests while still achieving the best combination of factor levels. Consequently, the proppant transport process was optimized by conducting multi-factor and multilevel orthogonal experiments. In the first sand-addition stage, the effects of the following factors were considered: (a) fracturing fluid flow rate, (b) sand ratio, (c) proppant size, (d) proppant density, (e) fracturing fluid viscosity and (f) fluid density. An orthogonal experimental design table L18 (6^3) was adopted, with 18 samples tested. The experimental design is listed in Table 1(No 1–18). When analyzing the influence of a particular factor on the proppant transport parameters, the average value of different experiments conducted under that specific factor was used for analysis. In addition, to achieve similarity in Reynolds number

Table 1
Experimental design table.

No	Fluid flow rate (m/s)	Sand ratio (%)	Proppant size (10^{-3}m)	Proppant density (kg/m^3)	Fluid viscosity (10^{-3} Pa s)	Fluid density (kg/m^3)
1	2	20	0.4	2700	3	1200
2	1	30	1.0	2700	3	1100
3	3	10	0.4	2700	5	1200
4	3	10	1.0	2700	1	1100
5	2	10	0.7	3400	5	1100
6	1	20	0.4	3400	5	1100
7	1	10	0.7	2000	3	1200
8	2	10	1.0	3400	3	1000
9	1	20	1.0	3400	1	1200
10	3	30	0.7	3400	1	1200
11	2	30	0.4	2000	1	1100
12	2	20	0.7	2700	1	1000
13	3	20	1.0	2000	5	1000
14	3	30	0.4	3400	3	1000
15	1	10	0.4	2000	1	1000
16	3	20	0.7	2000	3	1100
17	1	30	0.7	2700	5	1000
18	2	30	1.0	2000	5	1200
19	2	20	0.7	2700	3	1100
20	2	10	0.7	2700	3	1100
21	2	30	0.7	2700	3	1100
22	2	20	0.4	2700	3	1100
23	2	20	1	2700	3	1100
24	2	20	0.7	2000	3	1100
25	2	20	0.7	3400	3	1100
26	1	20	0.7	2700	3	1100
27	3	20	0.7	2700	3	1100
28	2	20	0.7	2700	1	1100
29	2	20	0.7	2700	5	1100

and linear velocity, the actual injection rates corresponding to fluid velocities of 1 m/s, 2 m/s, and 3 m/s in the numerical simulation are 1.17 m^3/min, 2.34 m^3/min, and 3.51 m^3/min, respectively. It should be noted that the actual hydraulic fractures consist of multiple clusters, while the experimental simulation represents only one cluster. Besides the injection rate, the sand ratio, proppant size, proppant density, fracturing fluid viscosity, and fracturing fluid density are consistent with actual field conditions.

In the second sand-addition stage, to enhance the longitudinal placement effect of the proppant, a simulation was conducted based on the model that exhibited the maximum sanding index in the first sand-addition stage. The sandbank equilibrium height was selected to indicate the placement effect in the second sand-addition stage. A controlled variable approach is adopted. The experimental design table is listed in Table 1(No 19–29).

2.4. Model verification

In this section, comparing the numerical simulation's results with those of previous physical experiments is crucial to ensure its accuracy. Previous studies on proppant transport primarily relied on the theory of the first sand-addition stage. Hence, this section presents a numerical simulation of continuous proppant transport and subsequently compares the findings with those obtained from prior physical experiments.

The accumulation of proppant was categorized into three stages in the fracture (YAJUN, L, 2006). As shown in Fig. 3a, in the first stage, the proppant settled, forming the initial shape of a sandbank. During the second stage, the height of the sandbank continued to increase. In the third stage, when the sandbank reached the equilibrium height, any subsequently injected proppant moved and settled at the back of the sandbank. Consequently, the length of the sandbank continued to increase while maintaining the same height. The numerical simulation results of this study are presented in Fig. 3b, representing the stages of formation, growth, balance, and extension of the sandbank. These results align with the trends of sandbanks observed in the physical experiments.

Another experimental results (HUI, F, 2017) is shown in Fig. 4a, while Fig. 4b displays the simulation results using the same parameters. Fig. 4c illustrates the high overall similarity between the shapes of the sandbank obtained from the physical experiment and numerical simulation. The sandbank equilibrium height obtained from the numerical simulation was slightly smaller than that obtained from the physical experiments, with an error of approximately 10%, because the proppant size used in the numerical simulation was an average value, whereas the particle size of the proppant used in the physical experiments varied within a range. This discrepancy in the proppant size can influence the formation of the sandbank and contribute to the variation in the

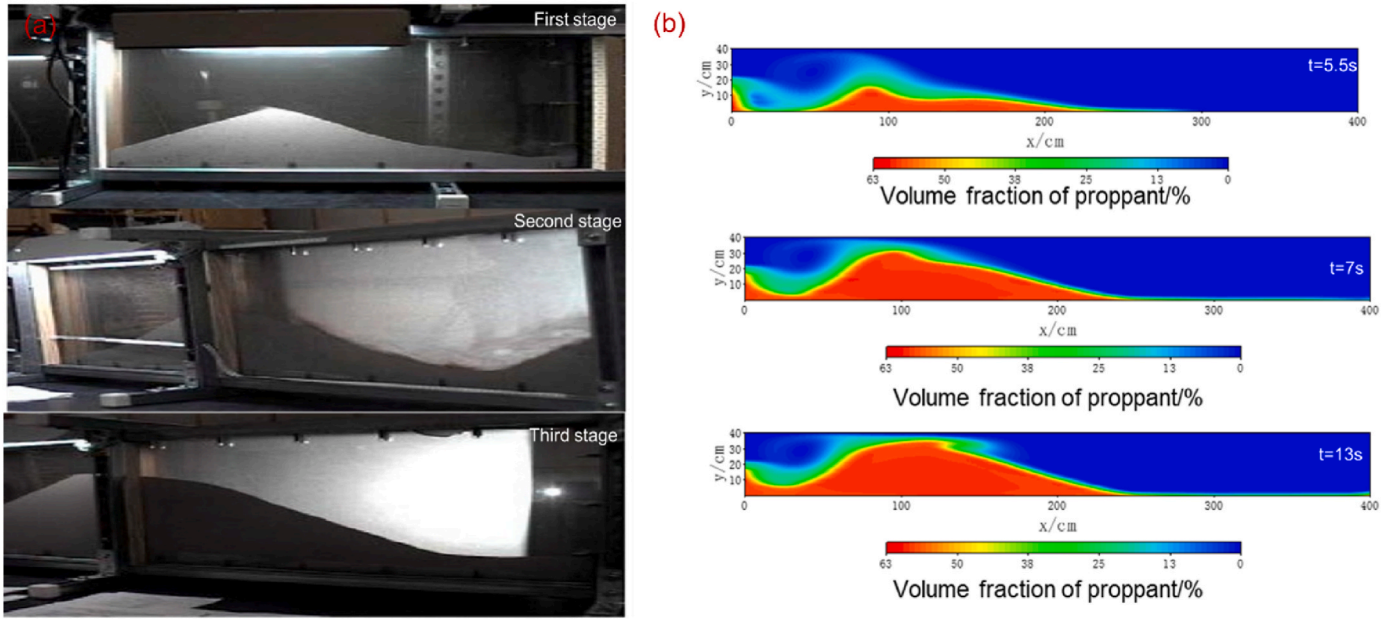

Fig. 3. Experimental and numerical simulation results: (a) Visualized proppant placement in the experiment (b) Simulated proppant placement by Eulerian- Eulerian multiphase model.

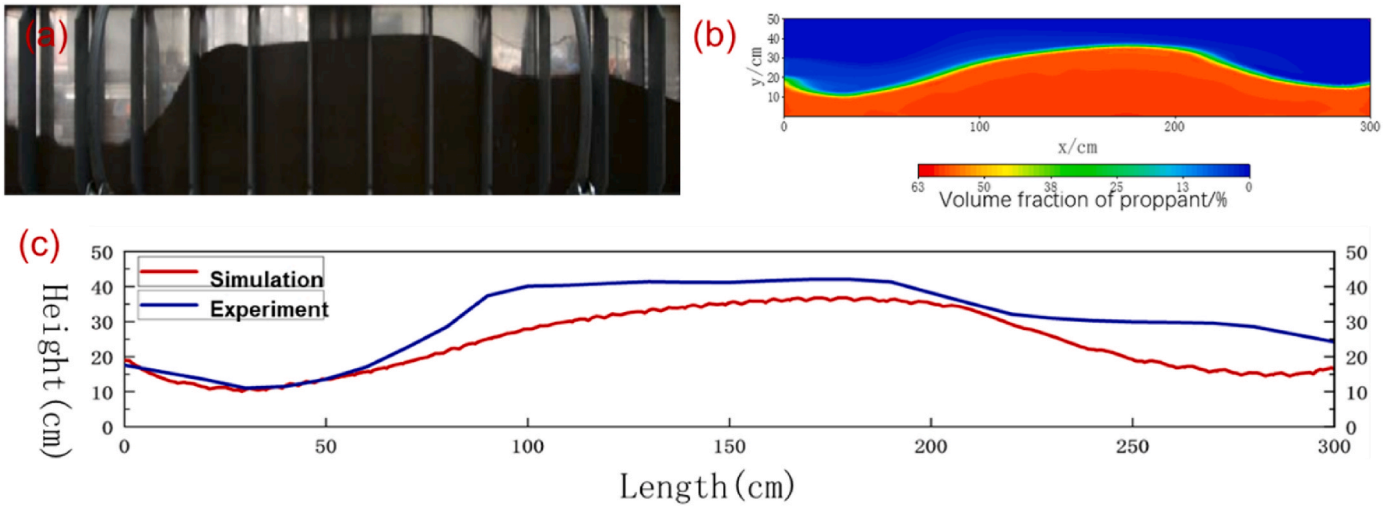

Fig. 4. Experimental and numerical simulation results: (a) Visualized proppant placement in experiment (b) Simulated proppant placement by Eulerian- Eulerian multiphase model, (c) The sandbank curve in experimental and numerical simulation.

equilibrium height. Furthermore, the physical experimental equipment affected the injection rate of the fracturing fluid, resulting in its actual speed being lower than the design flow rate. The flow rate of the fracturing fluid is negatively correlated with the sandbank equilibrium height, which can also lead to differences in the results of the physical and numerical experiments.

After comparing the simulation results with previous studies, the Eulerian-Eulerian multiphase model was employed in this study to accurately simulate proppant placement within a fracture. Therefore, this study provides a foundation for studying the proppant placement in secondary sand fracturing.

3. Results and discussion

3.1. First sand-addition stage

3.1.1. Sanding index analysis

As shown in Fig. 5, for this comparison, No. 3, 11, and 6 were chosen to represent cases with low, medium, and high sanding indices, respectively, as shown in Fig. 5. When the sanding index was small, the proppant tended to be concentrated at the far end of the crack, resulting in a small sandbank area and equilibrium height. When the sanding index is moderate, the proppant distribution covers the middle area of the crack, leading to an increased sandbank area and equilibrium height. When the sanding index is at its highest, the proppant can be effectively placed in the near-wellbore area while extending this positive effect to the far-wellbore area, owing to the larger sandbank laying length. The research findings strongly indicate that the sanding index proposed in this study successfully and comprehensively assessed the distribution characteristics of proppant inside fractures, considering factors such as the sandbank equilibrium height, sandbank leading-edge length, and sandbank laying length. The sanding index significantly contributes toward understanding the effectiveness of proppant placement and its impact on fracture conductivity.

3.1.2. Single factor analysis

As shown in Fig. 6a, the sandbank leading-edge length and laying length exhibit a trend of first increasing and then stabilizing with an increase in the sand ratio. This behavior was influenced by the interparticle interactions of the proppant. The equilibrium height, which represents the stabilized height of the sandbank, increased with an increase in the sand ratio because a higher sand ratio leads to stronger proppant interactions, which requires a higher equilibrium flow rate to maintain the proppant suspension in the flow passage section and allow the fracturing fluid to reach the far end of the fracture. In addition, the sand ratio significantly impacts the sanding index, showing a trend of

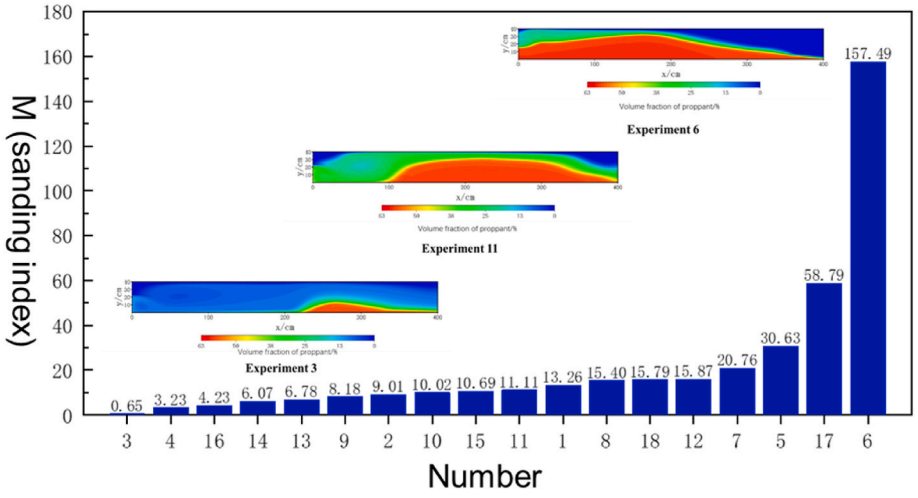

Fig. 5. Sanding index under different experiments in the first sand-addition stage.

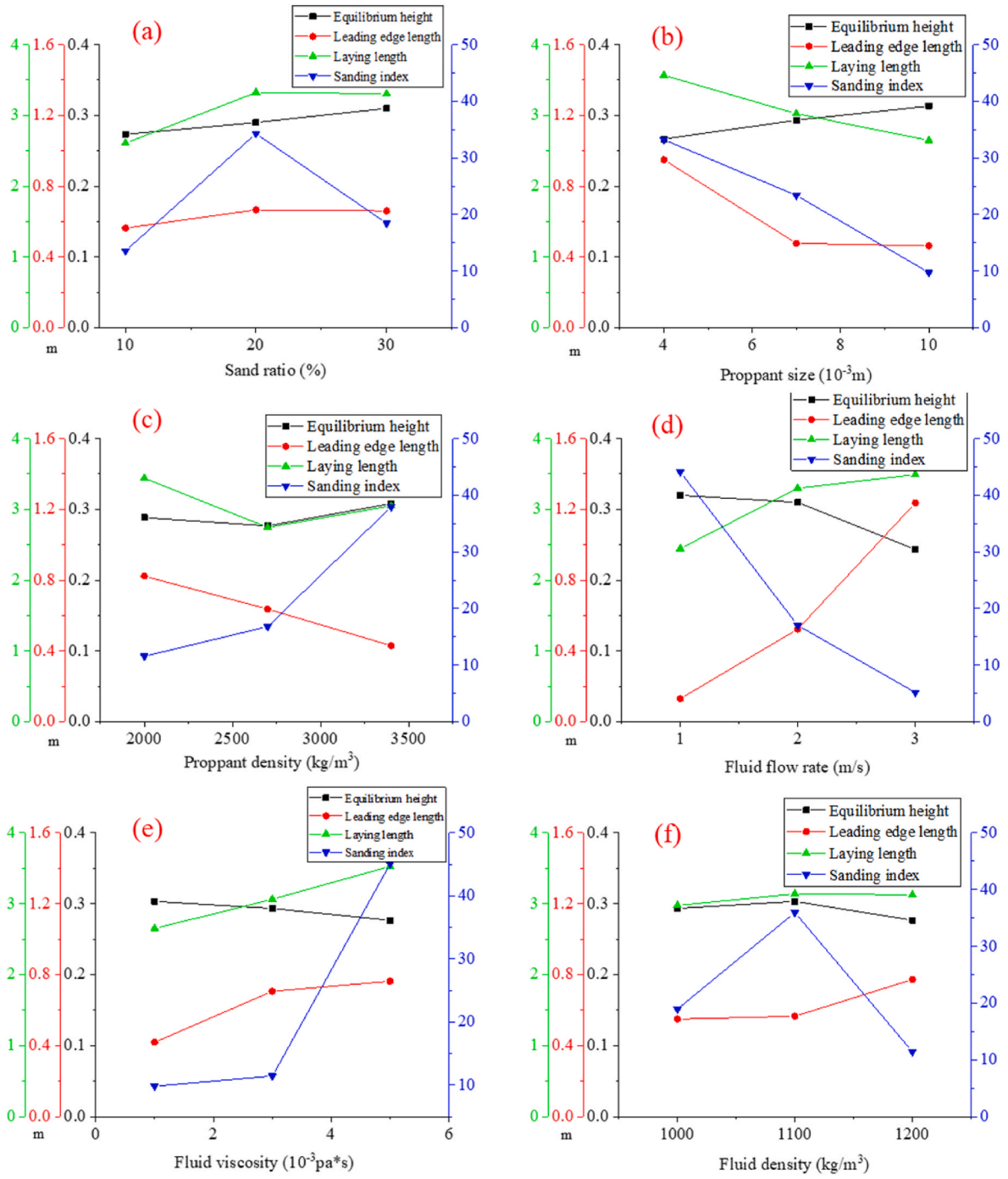

Fig. 6. Sensitivity analysis on proppant placement in first sand-addition stage (a) sand ratio effect, (b) proppant size effect, (c) proppant density effect, (d) fluid flow rate effect, (e) fluid viscosity effect and (f) fluid density effect.

first increasing and then decreasing with increasing sand ratio. An increase in the sand ratio was beneficial for filling the near-wellbore zone of the fracture with proppant. When the sand ratio became excessively large(>20%), the proppant settled quickly, leading to insufficient sand placement at the far end of the fracture.

As shown in Fig. 6b, the sandbank leading edge and laying lengths decrease with increasing particle size. The equilibrium height increased with increasing particle size owing to the accelerated sedimentation rate, necessitating an increase in the equilibrium level of the sandbank to satisfy the demand for a higher equilibrium flow rate of the fracturing fluid in the flow passage section. Moreover, the sanding index decreased with increasing proppant size because the larger particles settle more rapidly in the fracturing fluid, causing them to accumulate near the wellbore of the fracture quickly. Consequently, transporting these larger proppant particles to the far end of the fracture for proper laying and filling is challenging.

As shown in Fig. 6c, the sandbank leading edge length decreases quickly at higher proppant densitie. The laying length of the sandbank initially reduced and then increased with increasing proppant density because an increase in the proppant density leads to a higher settling speed, resulting in a decrease in the sanding distance. However, as the proppant density increased to 2700 kg/cm^3, the equilibrium flow rate increased, leading to an increase in the migration distance of the proppant at the back of the sandbank and an increase in the laying length.

The equilibrium height increases with increasing proppant density because a higher proppant density requires a smaller flow passage section to provide a higher equilibrium flow rate, which exerts a more significant drag force to transport the proppant to the far end of the crack. Furthermore, the sanding index improved with an increase in the proppant density as the settling speed of the proppant increased, leading to a more efficient filling effect in the near-wellbore zone of the fracture.

As shown in Fig. 6d, with an increase in the flow rate, the sandbank's leading-edge length and laying length exhibit an increasing trend. As the flow rate increased, the proppant experienced a more significant horizontal movement within the same settling time. A more substantial turbulence effect near the crack entrance at higher flow rates played an important role. The turbulence caused the settled proppant to be rolled up and carried further along the crack, contributing to the increased sandbank leading-edge length and laying distance. The higher the flow rate, the lower the equilibrium height. As the proppant settled and accumulated, the height of the sandbank within the fracture increased, occupying more space and reducing the available flow section of the fracturing fluid. Consequently, the flow rate of the fracturing fluid within the restricted area increases. When the flow rate of the fracturing fluid is increased beyond this equilibrium point, a larger flow section can accommodate the suspended proppant effectively, with the proppant remaining in the suspension without further settling. Consequently, the sandbank's equilibrium level decreased as the fracturing fluid's flow rate increased. Moreover, the sanding index decreases as the fluid flow rate increases. The proppant has a better filling effect at low flow rates in the near-wellbore zone, indicating that they are effectively distributed and placed around the wellbore area. However, as the flow rate of the fracturing fluid increases, turbulence and strong fluid flow can push proppant away from the wellbore, leading to inadequate support and coverage in that crucial area.

The settling speed of the proppant decreases with an increase in the fracturing fluid viscosity, leading to the proppant being easily carried to the far end of the fracture. As a result, both the sandbank leading edge and laying lengths increase with increasing fracturing fluid viscosity, as shown in Fig. 6e. Furthermore, an increase in the fluid viscosity leads to a decrease in the equilibrium height. An increase in viscosity amplified the horizontal velocity of the proppant decay more slowly, and the equilibrium velocity required for the proppant suspension state in the overflow section was lower. Consequently, an increase in the height of the overflow section led to a decrease in the equilibrium height. For the sanding index, increasing the viscosity on the proppant particles causes the settling velocity to decrease, and the attenuation rate of the horizontal motion velocity also decreases, resulting in a larger and more uniform settling distribution area for the proppant within the crack. Ultimately, an increase in the viscosity improves the sanding index.

In Fig. 6f, the sandbank leading-edge length increases with the fracturing fluid density, whereas the laying length does not change significantly with the fracturing fluid density. According to Stokes' law, the settling velocity of the proppant is directly proportional to the density contrast between the solid and liquid phases. Therefore, as the fracturing fluid's density increased, the proppant's settling velocity decreased. The increase in the fracturing fluid density affected the distance between the front edge of the sandbank and the distance between the sand spreading. Furthermore, the drag force of the fracturing fluid on the proppant increases as the fracturing fluid density increases. This increased drag force led to a decrease in the equilibrium flow rate. Consequently, the equilibrium height decreased with increasing fracturing fluid density. The sanding index follows a trend of first increasing and then decreasing as the density of the fracturing fluid increases. This pattern occurred because the sand-carrying capacity of the fluid was weak at low fracturing fluid density water levels. The proppant settles and accumulates near the wellbore, leading to difficulties in transporting it to the far end of the crack and effectively filling the area. As the fracturing fluid's density increases, the proppant's filling effect at the far end of the crack improves. However, when the density of the fracturing fluid was excessively high, the fluid had a high sand-carrying capacity, resulting in a larger distance from the front edge of the sandbank, implying that the near-wellbore area of the fracture was not filled effectively.

3.1.3. Range analysis

Range analysis is a statistical method used to assess the sensitivity of factors to the experimental results based on orthogonal experiments. The range analysis results for the sandbank leading edge length, equilibrium height, laying length, and sanding index from the orthogonal experiments are presented in Fig. 7, wherein larger values indicate a more significant impact of the respective factors on proppant placement. The sandbank leading-edge length, sandbank equilibrium height, sandbank laying length, and sanding index are primarily influenced by the fracturing fluid flow rate. In contrast, the fracturing fluid density has a relatively minor effect during the first sand-addition stage.

3.2. Second sand-addition stage

From Section 3.1, Experiment 6 in the first sand-addition stage showed the highest Sanding index. The geometric shape of the sandbank observed in Experiment 6 when it reached dynamic equilibrium served as the boundary condition for studying the influences of the proppant and fracturing fluid parameters on the sandbank equilibrium height in the second sand-addition stage. In addition, the density of fracturing fluid has a relatively small impact on the proppant transport 1. Therefore, in the second sand addition stage, the influence of fracturing fluid density was ignored.

3.2.1. Single factor analysis

As seen in Fig. 8a, when the sand ratio is at a lower level, the proppant undergoes a significant settlement and accumulation to form a second sandbank at the front and back of the primary sandbank; however, no apparent sandbank formation is observed at the upper part of the primary sandbank because, with a lower sand ratio, the intergranular interaction of the proppant is weaker. The cross-sectional area of the flow section at the front and back of the primary sandbank is larger, resulting in a lower average flow velocity of the fracturing fluid, thus making the proppant more prone to settling and accumulation. However, in the upper part of the primary sandbank, the cross-sectional area was smaller, leading to a higher average flow velocity of the fracturing fluid, making the proppant less likely to settle and remain suspended. As the sand ratio increased, the agglomeration and settlement of the proppant particles became stronger, resulting in a higher proppant settling velocity. Consequently, the proppant accumulated and settled in the front and upper parts of the primary sandbank, causing an upward trend in the equilibrium height of the sandbank. In addition, the proppant accumulates and settles near the crack entrance, forming a small sandbank.

According to Fig. 8b with an increase in particle size, the main area of proppant placement moves towards the near-wellbore zone of the fracture, and the equilibrium height shows an initial increase, followed by a decrease. This is because when the particle size is higher, the increase in the height of the front edge changes the flow field in the near-wellbore zone of the fracture. The upper part of the primary sandbank was significantly influenced by the turbulence at the crack entrance, leading to a decrease in the equilibrium height.

According to Fig. 8c, with the increase of proppant density, the main area of proppant placement moves towards the near-wellbore zone of the fracture, and the trend of equilibrium height shows an initial increase followed by a decrease. This is because when the proppant density is at a higher level, the increase in the height of the front edge changes the flow field in the near-wellbore zone of the fracture. The upper part of the primary sandbank is significantly influenced by the turbulent effect at the crack entrance, leading to a decrease in the equilibrium height.

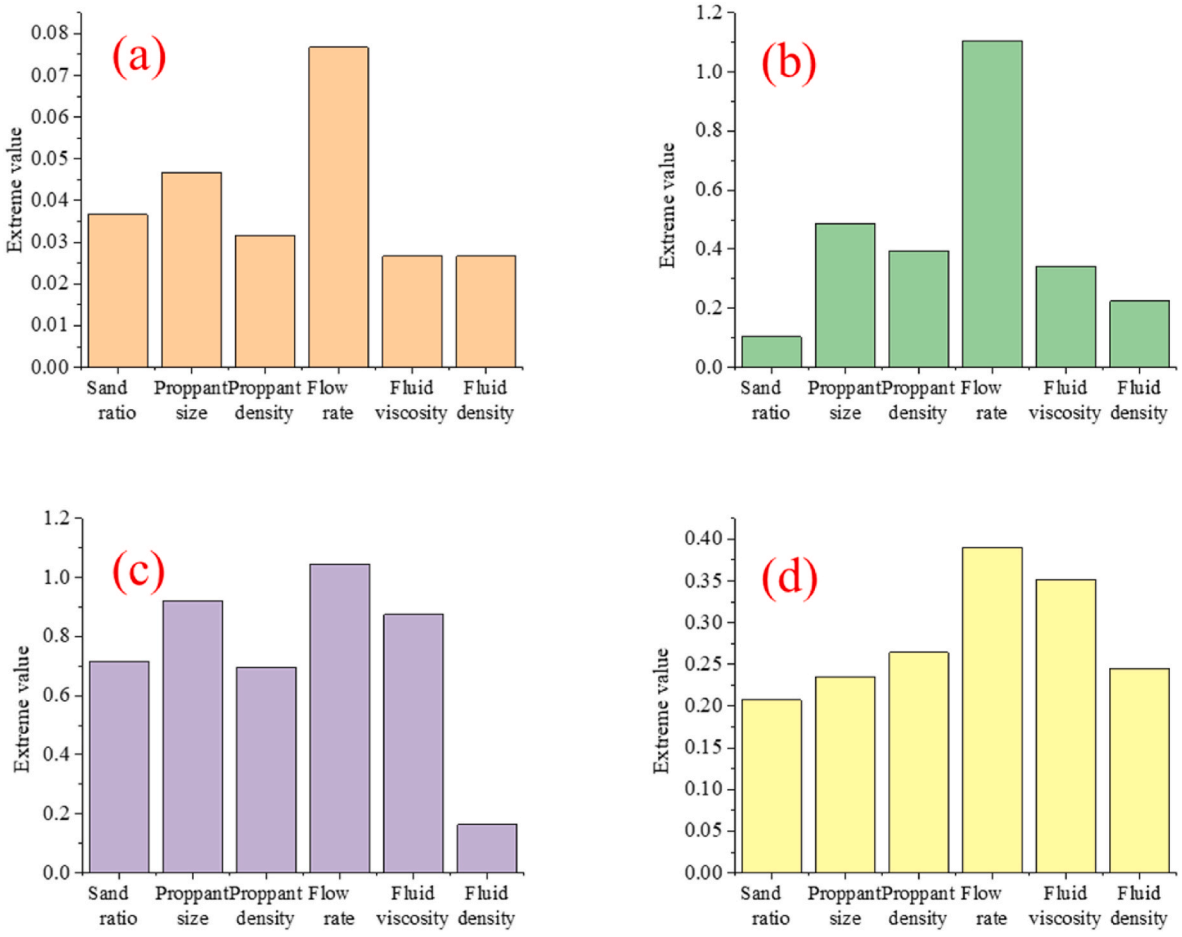

Fig. 7. Range analysis in the first sand-addition stage: (a) Equilibrium height, (b) Leading edge distance, (c) Laying length, (d) Sanding index.

According to Fig. 8d, when the flow velocity is low, the reduced carrying capacity of the fracturing fluid for the proppant leads to a higher equilibrium height of the sandbank. When the sandbank reaches an equilibrium state, a small sandbank is formed by the proppant in the far-wellbore zone of the fracture, which can improve proppant penetration and stimulation in the longitudinal and far-wellbore zones of the fracture. However, a sandbank's excessively high equilibrium height may lead to sand plugging. When the flow velocity of the fracturing fluid is high, the carrying capacity of the fracturing fluid for the proppant increases, leading to a decrease in the equilibrium height of the sandbank until it matches the morphological parameters of the primary sandbank.

According to Fig. 8e, the carrying capacity of the fracturing fluid for the proppant increased with an increase in the fracturing fluid viscosity, and its impact on the equilibrium height followed the same pattern as that of the proppant placement in the first sand-addition stage. The higher the viscosity of the fracturing fluid, the lower the equilibrium height.

3.2.2. Grey relational analysis

The degree of influence of each influencing factor on the proppant transport during the second sand-addition stage was different, thus making it necessary to conduct a sensitivity analysis on the influencing factors. In this section, the grey relational analysis method is used to determine the influence weight of each factor on the proppant (LU, C et al., 2022; SONG, Z et al., 2024; ZHANG, H et al., 2016). The specific implementation steps are as follows:

Perform dimensionless processing:

$$X_i(n) = \frac{x_i(n)}{\overline{x_i}} \tag{14}$$

Solving for the grey relational coefficient:

$$\xi_i(k) = \frac{\min\limits_i \min\limits_k |X_0(k) - X_i(k)| + \rho \max\limits_i \max\limits_k |X_0(k) - X_i(k)|}{X_0(k) - X_i(k) + \rho \max\limits_i \max\limits_k |X_0(k) - X_i(k)|} \tag{15}$$

Solve the correlation degree:

$$\gamma_i = \frac{1}{N} \sum_{k=1}^{N} \xi_i(k) \tag{16}$$

Solve for the weight coefficient:

$$W_i = \frac{\gamma_i}{\sum\limits_{i=1}^{n} \gamma_i} \tag{17}$$

where $X_i(k)$ is the dimensionless mean value of the i_{th} parameter, i is the parameters of the serial number, k is the data serial number, $x_i(k)$ is the i_{th} parameter value, $\overline{x_i}$ is the arithmetic mean, $\xi_i(k)$ is the grey relational coefficient, ρ is the distinguishing coefficient, taking a value of 0.5, γ_i is the degree of correlation degree, and W_i is the weight coefficient.

Fig. 9 indicates that during the second sand-addition stage, the weight coefficients of the different factors on the sandbank equilibrium height were comparable at approximately 0.2, indicating that these factors had comparable influences on the proppant placement effect. In practical terms, it is crucial to focus on the influence of construction parameters on specific aspects such as proppant embedment, propped-fracture conductivity, construction economy, and safety.

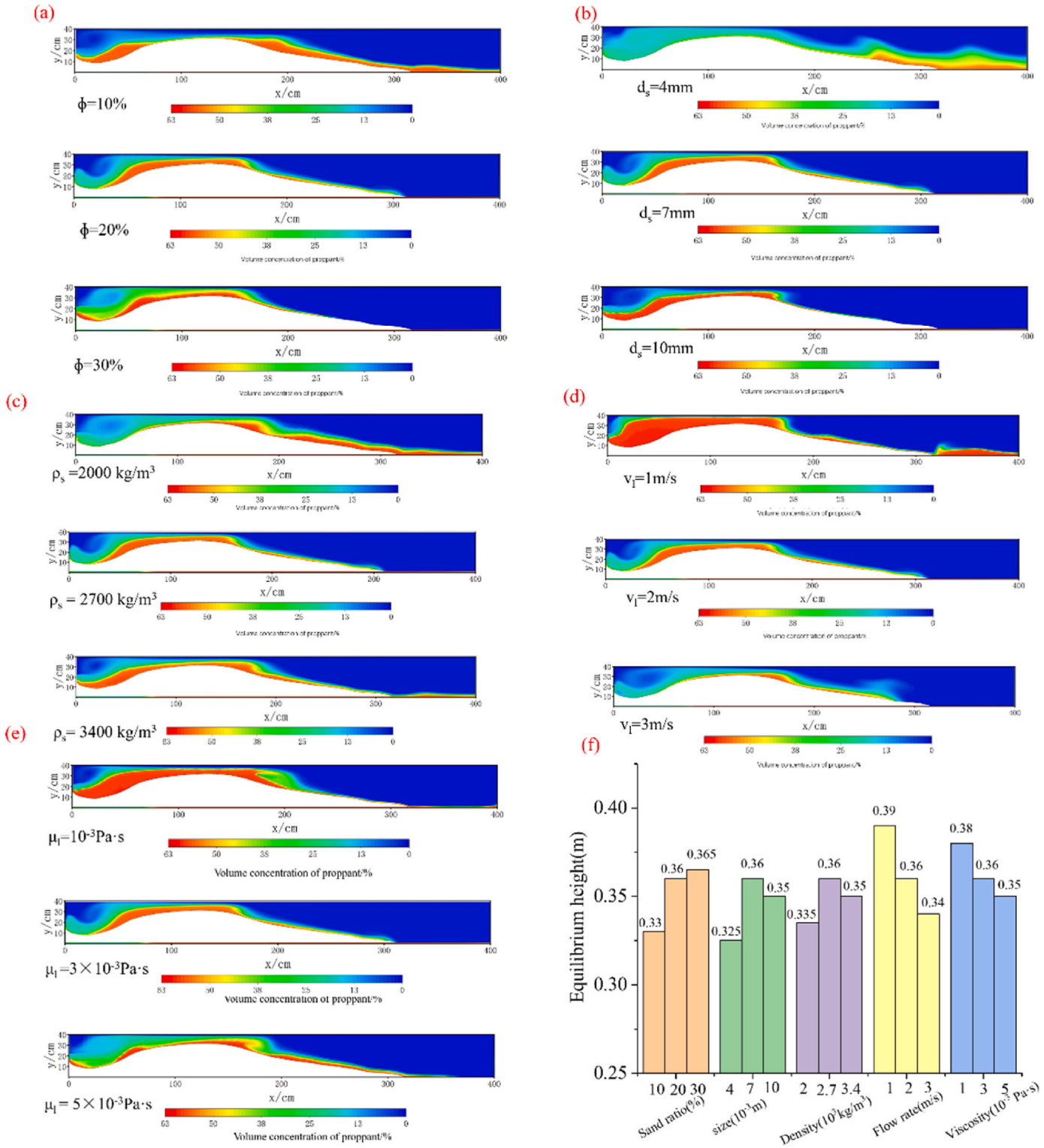

Fig. 8. The proppant distribution in the second sand-addition stage (a) sand ratio effect, (b) proppant size effect, (c) proppant density effect, (d) fluid flow rate effect, (e) fluid viscosity effect, (f) Equilibrium height statistical results.

4. Conclusion

In this study, an Eulerian-Eulerian multiphase model was established to simulate proppant transport in secondary sand fracturing for the first time, particularly considering the impact of artificial barriers formed in the first sand-addition stage on the proppant placement in the second sand-addition stage. Previous physical experiments were conducted to verify the reliability of the model. The effects of proppant performance, fracturing fluid performance, and fluid flow rate on proppant placement were analyzed. The following conclusions were drawn from this study.

(1) In the first sand-addition stage, an innovative sanding index was proposed to evaluate the effectiveness of proppant placement. The sanding index decreases with an increase in the proppant size

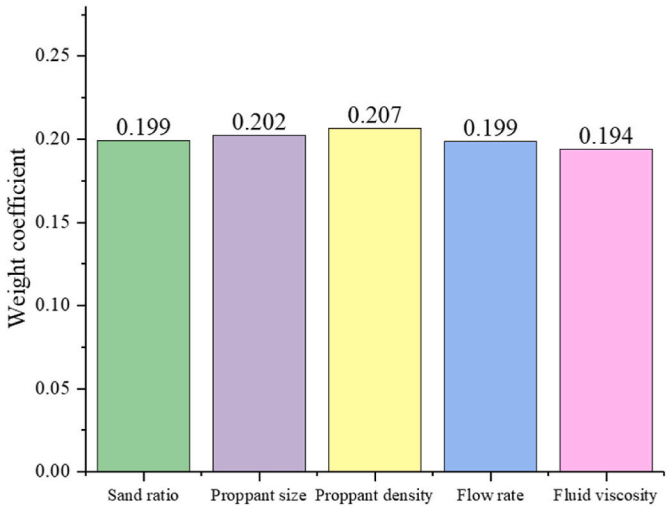

Fig. 9. Weight coefficient in the second sand-addition stage.

and flow rate and increases with an increase in the proppant density and fluid viscosity. With an increase in sand ratio and fluid density, the sanding index first increased and then decreased.

(2) In the first sand-addition stage, range analysis showed that the flow rate of the fracturing fluid had a greater impact on the proppant placement. In contrast, the density of the fracturing fluid had a more minor effect in the first sand-addition stage.

(3) In the second sand-addition stage, the artificial barrier formed in the first sand-addition stage was used as the boundary to analyze proppant placement. Notably, the equilibrium height increases with the increase of sand ratio, decreases with the increase of flow rate and fluid viscosity, and first increases and then decreases with the increase of particle size and proppant density.

(4) In the second sand-addition stage, the grey correlation method revealed that different factors had similar effects on proppant placement during the second sand-addition stage.

In summary, this study enriches the research on the proppant transport in hydraulic fracturing, especially providing a more scientific and reasonable theoretical design basis for secondary sand fracturing. Future research also needs to consider the proppant transport under the dynamic expansion of cracks in secondary sand fracturing.

CRediT authorship contribution statement

Huohai Yang: Resources, Project administration, Methodology, Formal analysis, Conceptualization. **Kuncheng Li:** Resources, Project administration, Methodology, Formal analysis, Conceptualization. **Zijia Liao:** Writing – review & editing, Writing – original draft, Validation, Supervision. **Xiaogang Li:** Writing – review & editing, Validation, Supervision. **Hesamoddin Rabiee:** Writing – review & editing, Project administration. **Shirui Ren:** Software, Methodology, Investigation. **Xinwei Luo:** Software, Methodology, Investigation. **Qingyuan Chen:** Writing – review & editing, Validation, Supervision. **Lei Ge:** Writing – review & editing, Writing – original draft, Validation, Supervision. **Hao Wang:** Writing – review & editing, Project administration.

Declaration of competing interest

The authors declare that they have no known competing financial interests or personal relationships that could have appeared to influence the work reported in this paper.

Data availability

Data will be made available on request.

Acknowledgment

This project was supported by the Tianfu Yongxing Laboratory Organized Research Project Funding (No. 2023CXXM01), and the Opening Project of the Oil and Gas Field Applied Chemistry Key Laboratory of the Sichuan Province (YQKF202203). The authors also acknowledge the support from Australia Research Council Linkage project (LP200100420).

References

Abdin, Z., 2024. Bridging the energy future: the role and potential of hydrogen co-firing with natural gas. J. Clean. Prod. 436, 140724.
Bingwei, X.U., Shibin, W., Chengcheng, L., 2022. Research and application of water-control secondary sanding fracturing technology in tight low permeability bottom water gas reservoir. Reservoir Evaluation and Development 12 (4), 698–702 (In Chinese).
Cao, H., Li, Z., Gao, Q., Chen, J., Sun, P., Erneste, H., 2024. The characterization of incline-induced flow conductivity in shale's proppant-packed crack: lab-scale study. Fuel 357, 129675.
Chen, B., Barboza, B.R., Sun, Y., Bai, J., Thomas, H.R., Dutko, M., Cottrell, M., Li, C., 2022. A review of hydraulic fracturing simulation. Arch. Comput. Methods Eng. 29 (4), 1–58.
Feng-Sheng, Y., Bing, C., Shu-Bin, W., Zhong-Tai, H.U., Yu, X., Liang, T., 2020. Application of secondary sand fracturing technique in offshore low porosity and permeability sandstone gas reservoir. Sci. Technol. Eng. 20 (14), 5615–5621 (In Chinese).
Gong, Y., Mehana, M., El-Monier, I., Viswanathan, H., 2020. Proppant placement in complex fracture geometries: a computational fluid dynamics study. J. Nat. Gas Sci. Eng. 79, 103295.
Gong, F., Gao, L., Zou, G., Peng, S., Song, Y., 2023. The investigation of multiple factors on elastic anisotropy of artificial shale based on the orthogonal experiment. Petrol. Sci. 20 (5), 2773–2783.
Guo, T., Luo, Z., Zhou, J., Gong, Y., Dai, C., Tang, J., Yu, Y., Xiao, B., Niu, B., Ge, J., 2022. Numerical simulation on proppant migration and placement within the rough and complex fractures. Petrol. Sci. 19 (5), 2268–2283.
Hui, F., 2017. Study on the Rule of Proppant Displacement in Fractures of Slickwater Fracturing[D]. Xi'an Shiyou University.
Lai, F., Li, Z., Wang, Y., 2017. Impact of water blocking in fractures on the performance of hydraulically fractured horizontal wells in tight gas reservoir. J. Petrol. Sci. Eng. 156, 134–141.
Li, Y., Dong, S., Guo, J., Li, C., Zhao, J.. The Theoretical Research of Secondary Sand Fracturing and Application in Fields. https://doi.org/10.2118/2009-121.
Li, X., Hao, J., 2020. Optimization design of low-density and high-strength ceramic proppants by orthogonal experiment. Adv. Compos. Lett. 29, 2633366X2095487.
Li, H., Huang, B., Zhao, X., Wu, Z., Han, X., Jiao, X., Sun, Z., 2022. Experimental investigation on proppant transport and distribution characteristics in coal hydraulic fractures under true triaxial stresses. J. Petrol. Sci. Eng. 218, 110993.
Li, H., Huang, B., Han, X., Wu, Z., Li, H., Zhao, X., 2023. Pulse effects on proppant transport and dune shape in vertical fracture applied in coalbed methane mining engineering during the pulse hydraulic fracturing. Geoenergy Science and Engineering 229, 212128.
Liao, Z., Li, X., Ge, L., Yang, Z., Zhu, J., Xue, Q., Wang, H., 2022. Lightweight proppants in unconventional oil and natural gas development: a review. Sustainable Materials and Technologies 33, e484.
Lu, C., Liu, J., Huang, F., Wang, J., Zhou, G., Wang, J., Meng, X., Liu, Y., Wang, X., Shan, X., Liang, H., Guo, J., 2022. Numerical simulation of proppant embedment in rough surfaces based on full reverse reconstruction. J. Pet. Explor. Prod. Technol. 12 (9), 2599–2608.
Mao, S., Siddhamshetty, P., Zhang, Z., Yu, W., Chun, T., Kwon, J.S., Wu, K., 2020. Impact of proppant pumping schedule on well production for slickwater fracturing. SPE J. 26 (1), 342–358.
Mao, S., Wu, K., Moridis, G., 2023. Integrated simulation of three-dimensional hydraulic fracture propagation and Lagrangian proppant transport in multilayered reservoirs. Comput. Methods Appl. Mech. Eng. 410, 116037.
Prasun, S., Ghalambor, A., 2018. Effect of multi-stage hydraulic fractures on performance of naturally fractured tight oil reservoirs with bottom-water[Z]. Lafayette, Louisiana, USA.
Raimbay, A., Babadagli, T., Kuru, E., Develi, K., 2016. Quantitative and visual analysis of proppant transport in rough fractures. J. Nat. Gas Sci. Eng. 33, 1291–1307.
Sanya, C., Konisky, D.M., 2020. The justice and equity implications of the clean energy transition. Nat. Energy 5 (8), 569–577.
Shi, F., Wang, X., Liu, C., Liu, H., Wu, H., 2018. An XFEM-based numerical model to calculate conductivity of propped fracture considering proppant transport, embedment and crushing. J. Petrol. Sci. Eng. 167, 615–626.
Song, Z., Lv, M., Zhao, L., Liu, C., He, Y., Zhang, Y., Lobusev, M.A., 2024. A novel bound water occurrence model for tight sandstone. Fuel 357, 130030.

Suri, Y., Islam, S.Z., Hossain, M., 2019. A new CFD approach for proppant transport in unconventional hydraulic fractures. J. Nat. Gas Sci. Eng. 70, 102951.
Tiankui, G., Xing, Y., Hai, L., Ming, C., Zunpeng, H., Jilei, N., Yiman, S., 2023. Numerical simulation of proppant transport from a horizontal well into a perforation using computational fluid dynamics. Nat. Gas. Ind. B 10 (4), 341–351.
Wen, Q., Wang, S., Duan, X., Li, Y., Wang, F., Jin, X., 2016. Experimental investigation of proppant settling in complex hydraulic-natural fracture system in shale reservoirs. J. Nat. Gas Sci. Eng. 33, 70–80.
Wen, Z., Zhang, L., Tang, H., Zeng, J., He, X., Yang, Z., Zhao, Y., 2022. A review on numerical simulation of proppant transport: Eulerian–Lagrangian views. J. Petrol. Sci. Eng. 217, 110902.
Yajun, L., 2006. Settling and Hydrodynamic Retardation of Proppants in Hydraulic fractures[D]. The university of Texas at Austin.
Yang, R., Guo, J., Zhang, T., Zhang, X., Ma, J., Li, Y., 2019. Numerical Study on Proppant Transport and Placement in Complex Fractures System of Shale Formation Using Eulerian Multiphase Model Approach[Z]. Beijing, China.
Yi, S.S., Wu, C., Sharma, M.M., 2018. Proppant distribution among multiple perforation clusters in plug-and-perforate stages. SPE Prod. Oper. 33 (4), 654–665.
Zeng, J., Li, H., Zhang, D., 2019. Numerical simulation of proppant transport in propagating fractures with the multi-phase particle-in-cell method. Fuel 245, 316–335.
Zhang, H., Wang, J., Zhang, H., 2016. Investigation of the main factors during shale-gas production using grey relational analysis. Open Petrol. Eng. J. 9 (1), 207–215.
Zhang, J., Li, Y., Yang, H., Guo, X., 2023. Simulation and analysis of proppant transport patterns in wellbore-fracture systems. Energies 16 (11), 4421.
Zhao, J., Li, T., Shi, Y., An, C., Liu, Y., 2019. A new sinking agent used in water-control fracturing for low-permeability/bottom-water reservoirs: experimental study and field application. J. Petrol. Sci. Eng. 177, 215–223.
Zou, G., Xu, J., Wu, C., 2017. Evaluation of factors that affect rutting resistance of asphalt mixes by orthogonal experiment design. International Journal of Pavement Research and Technology 10 (3), 282–288.